Chapter 1

The Nature of High Temperature Oxidation

At high temperatures, most metals will inevitably oxidise over a wide range of conditions. The practical issues of material lifetimes and corrosion protection methods therefore centre around the rate of oxidation, and how to control reaction morphology. Answers to the second question turn out to be rather interesting and involve the need for a fundamental understanding of the processes involved and ways to modify them. The general nature of the problem can be appreciated from a consideration of some practical examples.

1.1 METAL LOSS DUE TO THE SCALING OF STEEL

Carbon steel is produced in prodigious quantities (about 1.7×10^9 t worldwide in 2014). Almost all of it is cast into large pieces such as slabs, which are subsequently reheated to around 1000−1200°C to be formed into more useful shapes (Fig. 1.1). The reheating operation is carried out in direct fired furnaces where steelworks gases, or sometimes natural gas, are combusted with excess air. The combination of high temperature, heating times of around two hours, and oxidising gases leads to the growth of a thick iron oxide scale on the steel. The amount of steel consumed in this way is about 1−2% of the total. Obviously, with steel losses of 17−34 Mt in 2014, plus the added cost of removing the scale and recycling it, there is considerable economic motivation to control or slow this process. However, there are difficulties.

As discussed later, and as is intuitively reasonable, the steel scaling rate depends on three variables: steel chemistry, temperature and the gas

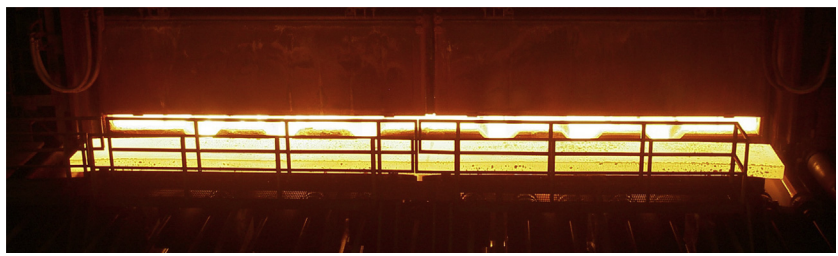

FIGURE 1.1 Oxidised steel slab emerging from reheat furnace. *Courtesy of BlueScope Steel.*

High Temperature Oxidation and Corrosion of Metals. http://dx.doi.org/10.1016/B978-0-08-100101-1.00001-7

atmosphere. The first cannot be changed, because it is critical to the final steel properties. Temperature is determined by steel chemistry and is therefore also fixed. Changes in gas composition should, however, be possible. The reactions producing the furnace atmospheres can be described as

$$CH_4 + \frac{3+x}{2}O_2 = CO + 2H_2O + \frac{x}{2}O_2 \qquad [1.1]$$

and

$$CO + \frac{1+x}{2}O_2 = CO_2 + \frac{x}{2}O_2 \qquad [1.2]$$

where x represents the surplus of oxygen above stoichiometric requirements for complete combustion. In normal practice, excess air ($x > 0$) is used to ensure complete combustion. However, it was recognised long ago [1] that for $x < 0$, the atmosphere would be much less oxidising and the extent of scaling might thereby be lessened.

In analysing this suggestion, we recognise that it is necessary to calculate the furnace gas partial pressure of oxygen, p_{O_2}, as a function of x and temperature, that the possible oxides of iron must be identified, and that the ranges of p_{O_2} values at which they exist need to be established. The necessary p_{O_2} values can be calculated from the equilibrium of reactions [1.1] and [1.2] and those of the iron oxide formation reactions, using the techniques of chemical thermodynamics described in Chapter 2. Such an analysis shows that it is not possible to lower p_{O_2} below the value at which iron oxidises and still have sufficient combustion to heat the steel. Given that steel scaling cannot be prevented, it is important to know how the rate of scale growth (and steel consumption) varies with p_{O_2} and temperature.

A schematic cross-sectional view of a growing oxide scale is shown in Fig. 1.2. The overall oxidation process can be subdivided into several steps:

1. Delivery of oxidant to the scale−gas interface via mass transfer in the gas phase.
2. Incorporation of oxygen into the oxide scale.
3. Delivery of reacting metal from the alloy to the alloy−scale interface.
4. Incorporation of metal into the oxide scale.
5. Transport of metal and/or oxygen through the scale.

Evaluation of the rates at which these steps occur involves calculation of the gas phase mass transfer, solid-state mass transfer or diffusion in the oxide and alloy and consideration of the interfacial redox reactions

$$Fe = Fe^{n+} + ne^- \qquad [1.3]$$

$$2e^- + \frac{1}{2}O_2 = O^{2-} \qquad [1.4]$$

where e^- represents an electron. The redox reactions are rapid and do not usually contribute to rate control. Other scale−gas interactions can be dealt

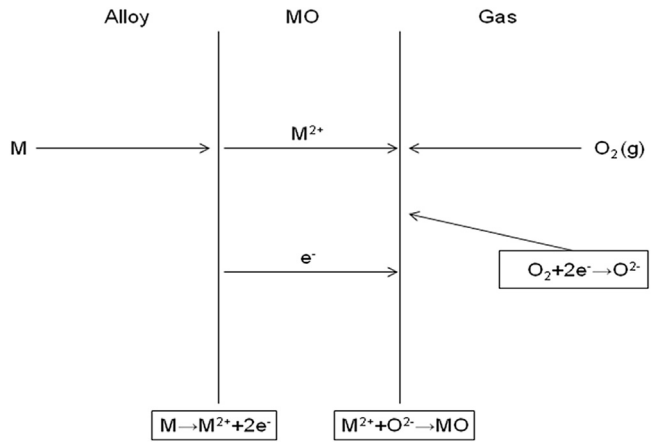

FIGURE 1.2 Reactions and transport processes involved in the growth of an oxide scale.

with using the methods of surface chemistry. Gas phase mass transfer rates can be calculated from the methods of fluid dynamics, whilst mass transfer in the solid oxide and alloy is described using diffusion theory.

The principal constituent of an iron oxide scale at $T > 570°C$ is wüstite, FeO, in which the Fe^{2+} species diffuses rapidly at high temperatures. At high values of p_{O_2}, diffusion in FeO controls the rate at which this oxide accumulates [2]. However, in a combustion gas, where p_{O_2} can be quite low, reaction with the oxidant species CO_2 and/or H_2O is slower than wüstite diffusion, and controls the scaling rate [3]. Thus it appears possible that steel scaling can be slowed by operating reheat furnaces under substoichiometric combustion conditions. Of course, the economic feasibility of this process alteration would have to be established through quantification of the actual benefit to be expected (as well as the costs). Such an exercise requires the ability to predict scaling rates as a numerical function of process variables, a principal concern of this book.

1.2 HEATING ELEMENTS

The use of metals as electrical resistance heating elements is commonplace in small domestic appliances and laboratory furnaces. Of course the metals used must resist oxidation in air. Two groups of alloys are widely used for this purpose: nickel alloys containing around 20 w/o (weight percent) chromium and iron alloys containing about 20 w/o Cr and 5 w/o Al. As pure metals, each of Fe, Ni, Cr and Al oxidises in air, but at vastly different rates. Oxidation rate measurements are discussed later in this chapter, but for the moment, it is sufficient to use a comparison of different oxide scale thicknesses grown in a particular time. Data for 100 h reaction at 800°C in pure O_2 at 1 atm are shown in Table 1.1.

It is clear that pure iron would be quite unacceptable as a heating element, and that aluminium and chromium appear much more attractive. However,

TABLE 1.1 Metal Oxide Scale Thicknesses ($t = 100$ h, $p_{O_2} = 1$ atm, $T = 800°C$)

Metal	Scale Thickness/mm
Fe	1.1
Ni	0.01
Cr	0.003
Al[a]	0.001

[a]*Measured on Ni-50Al.*

these are not practical choices: aluminium melts at 660°C and pure chromium is brittle and cannot be formed at room temperature. Nickel has neither of these deficiencies and might have an acceptable scaling rate for some applications. However, like most metals in the pure state, nickel has quite poor high temperature strength and cannot be used. On the other hand, appropriate alloying can provide both strength and oxidation resistance.

Cross-sectional views of oxidised surfaces of Ni-28Cr and Fe-20.1Cr-5.6Al-0.08La alloys (all compositions in weight %) are shown in Fig. 1.3. Single-phase oxides, Cr_2O_3 and Al_2O_3, respectively, grow as almost uniform scales, providing satisfactorily slow alloy consumption rates. It would be useful to be able to predict what concentrations of chromium and aluminium are required to achieve their preferential oxidation and thereby avoid reaction of the nickel or iron. To deal with this situation, it will be necessary to consider the thermodynamics of competitive oxidation processes such as

$$2\underline{Cr} + 3NiO = Cr_2O_3 + 3\underline{Ni} \qquad [1.5]$$

where underlining indicates the metal is present as an alloy solute. An additional factor can be expected to complicate this prediction. Selective oxidation of a metal implies its removal from the alloy and a lowering of its concentration at the alloy surface. Thus it will also be necessary to consider the diffusion processes in both alloy and oxide.

1.3 PROTECTING TURBINE ENGINE COMPONENTS

The gas turbine engines used to propel aircraft and to generate electric power have been developed to a remarkable extent since their invention in the mid-20th century. As shown in Fig. 1.4, fuel is combusted within a turbine to produce a large volume of hot gas. This gas impinges on angled blades in the hot (turbine) stage of the engine, causing it to rotate and drive the compressor stage, which draws in air to support combustion. Power is obtained from the engine either as rotational energy via a driveshaft, or as thrust, generated by the jet of hot exhaust gas.

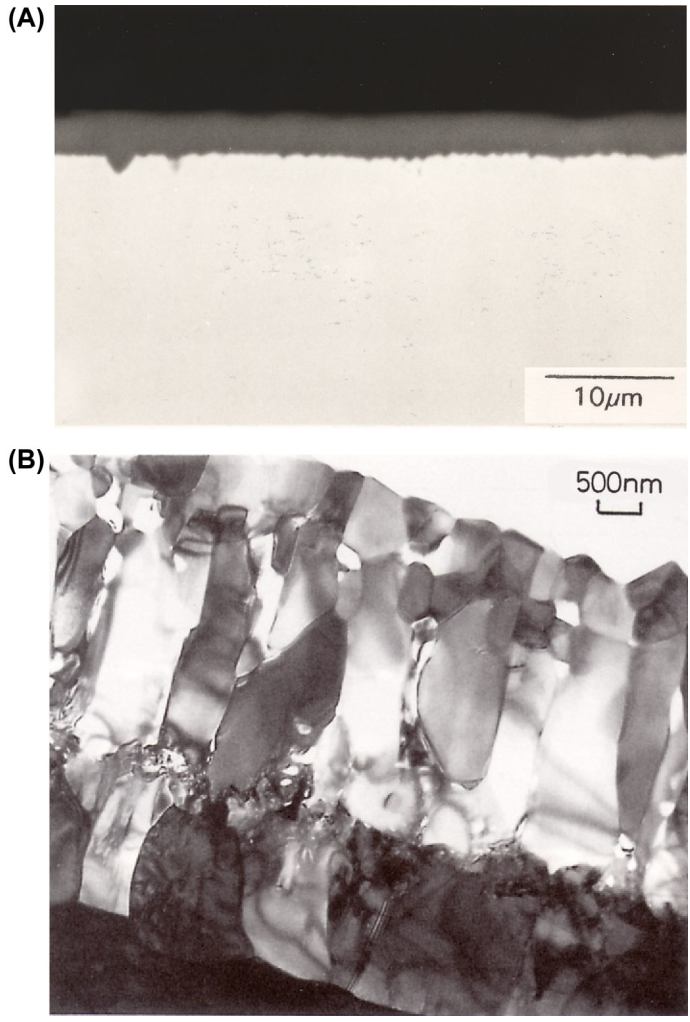

FIGURE 1.3 Cross-section of slow-growing protective scales: (A) Optical micrograph of Cr_2O_3 on Ni-28Cr after 24 h at 900°C and (B) Bright field transmission electron microscopy view of Al_2O_3 on Fe-20Cr-6Al-0.08La after 400 h at 1150°C [4]. *Published with permission of Science Reviews.*

The efficiency of the engine, which is the proportion of the thermal energy converted to mechanical power, is related to the theoretical maximum work available, given by

$$w_{\max} = \frac{T - T_o}{T} q \qquad [1.6]$$

where q is the heat exchanged, T_o is the ambient temperature and T the operating temperature. It is clear that the higher the turbine operation temperature, the

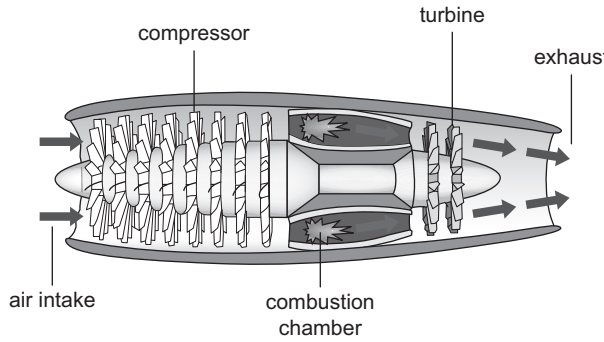

FIGURE 1.4 Schematic diagram of gas turbine engine.

greater is the efficiency potentially available. Since higher efficiency is the equivalent of lower cost and less greenhouse gas production per unit of output, its desirability has driven a steady increase in turbine gas temperatures. However, because this temperature is limited to whatever the materials of the first hot stage components can withstand, an increase in materials capability has also been necessary.

The history of developments in turbine blade materials and the temperatures at which they have operated are summarised in Fig. 1.1. In addition to alloy compositional changes, the development of these materials has seen an evolution in production technology from wrought through conventionally cast and directionally solidified to single crystal production. Current hot stage materials are nickel-based superalloys, which possess excellent high temperature strength. This is necessary to withstand the enormous centrifugal forces generated by the high rotational speeds, around 10,000 rpm in the case of jet engines. The metallurgical design which provides the strength of these superalloys is such that they oxidise at unacceptably rapid rates at operating temperature. This problem has been solved by providing a coating of oxidation resistant alloy on the component surfaces.

Turbine temperatures are now exceeding the capabilities of superalloy components, and it has become necessary to cool them. This is done by pumping air or steam through cooling channels running through the component interiors and providing thermal insulation (a thermal barrier coating or TBC) on top of the oxidation-resistant coating. The whole assembly is shown schematically in Fig. 1.6. The TBC is typically a ceramic made of Y_2O_3-stabilised ZrO_2; the oxidation resistant coating, known as a bond coat, is an aluminium-rich material (several designs are possible); and the superalloys are complex, nickel-based alloys containing chromium, aluminium and numerous other elements. Some examples of superalloy and bond coat compositions are given in Table 1.2. Additional superalloy compositions are shown in Appendix A.

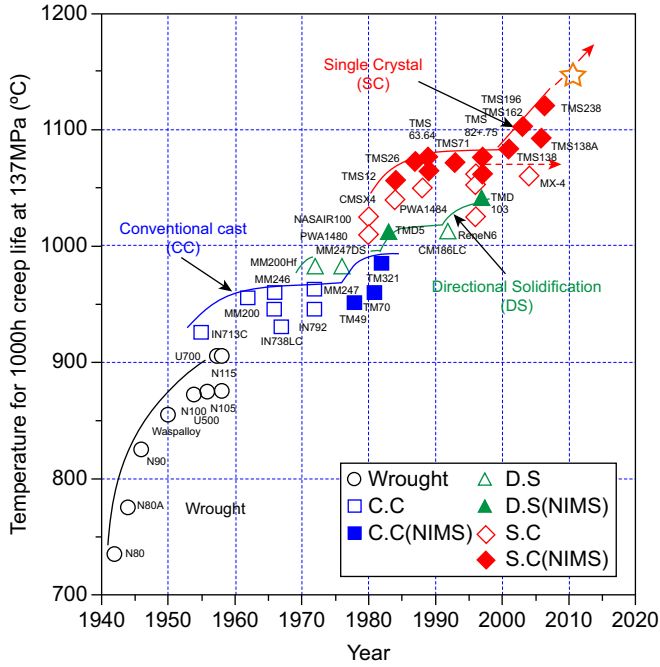

FIGURE 1.5 Progressive increases in temperature capabilities of superalloys for turbine engine blades. *Reproduced with permission of the National Institute of Materials (NIMS), Japan.*

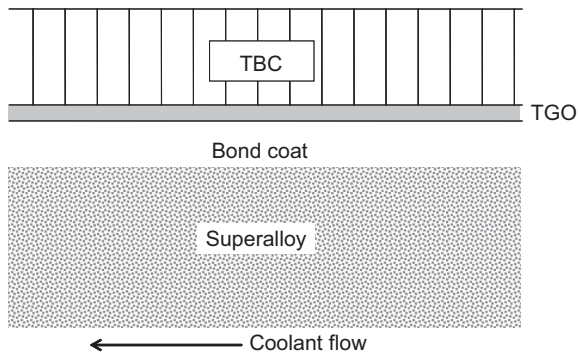

FIGURE 1.6 Cross-sectional view of TBC system for gas turbine blade.

Manufacture of these sophisticated components is complex. The superalloy itself is cast, using a directional solidification process, often as a single crystal [5]. The bond coat can be applied in various ways [6]. Chemical vapour deposition (CVD), in which aluminium from a vapour phase species diffuses into the alloy surface, forms an aluminide diffusion coating. These coatings can be modified by the incorporation of platinum and the codeposition of additional

TABLE 1.2 Some Superalloy and Coating Nominal Compositions (w/o)

Material	Ni	Cr	Al	Co	Mo	W	Ti	C	Other
IN738LC	bal	15.8	3.1	8.5	1.8	2.6	3.4	0.1	0.5Si, 0.8Ta
René N4	bal	10.3	4.2	7.8	1.5	6.4	3.5		0.47Nb, 4.6Ta
René N5	bal	7.5	6.2	7.7	1.4	6.4			7.1Ta, 2.8Re, 0.15Hf
CMSX4	bal	7.5	12.6	10.0	0.4	2.1	1.3	0.1	2.1Ta, 1Re, 0.03Hf
PWA 1480	bal	10	5	5		4	1.5		12Ta
PWA 1484	bal	5	5.6	10	2	6			8.7Ta, 3Re, 0.1Hf
MC2	bal	7.8	5.0	5.2	2.1	8.0			5.8Ta
SRR99	bal	9.6	12.0	5.0	0.3	3.0	2.7	0.1	0.9Ta
NiCoCrAlY[a]	bal	18	12.5	23					1Y
β-NiAl[b]	bal	7	30	5			2		

[a] *Overlay coating.*
[b] *Diffusion coating on René N4.*

metals from the vapour phase. More complex coating chemistries can be achieved by physical codeposition of various MCrAlY compositions in which M indicates Fe, Ni or Co, or a mixture thereof. These coatings are deposited by sputtering, plasma spraying or physical vapour deposition, using a high voltage electron beam to vapourise the source material. The outer surface of the bond coat is oxidised to form a thermally grown oxide (TGO) which is the surface to which the TBC adheres. The thermal barrier coating is deposited by either electron beam physical vapour deposition or plasma spraying [7].

At high temperatures, various interactions between these materials can be expected. Interdiffusion between the superalloy and its aluminium-rich coating can produce new phases as well as draining the coating of its essential aluminium. Some bond coat constituents and metals diffusing from the superalloy through the bond coat can dissolve in the TBC to form mixed oxides. Understanding and predicting these interactions requires knowledge of the phase equilibria relevant to each particular system. Finally, because the TBC is porous, oxygen from the hot combustion gas penetrates to the bond coat surface, causing oxide scale growth. A high degree of resistance to this oxidation process is an essential function of the bond coat. All of these processes are accompanied by volume changes, which have the potential to mechanically disrupt the junction between the TBC and the underlying oxide scale. This in turn can lead to partial or even complete loss of the TBC, subsequent overheating of the substrate metal and component failure. In order to predict and thereby manage these consequences, it is necessary to understand the detailed mechanics of stress development within the superalloy substrate-bond coat-TGO-TBC system and the ways in which that stress is accommodated by deformation or fracture of one or more of the system components.

1.4 HYDROCARBON CRACKING FURNACES

Many chemical and petrochemical processes are operated at high temperatures in order to achieve reasonable production rates or, as in cracking furnaces, to promote endothermic reactions. Cracking (or pyrolysis) furnaces are used to produce olefines such as ethylene and propylene, which are subsequently used to make the commodity materials polyethylene and polypropylene. The cracking reaction can be written

$$-CH_2-CH_2- = -CH{=}CH- + H_2 \qquad [1.7]$$

and is accompanied by carbon formation:

$$CH_4 = C + 2H_2 \qquad [1.8]$$

To slow the latter reaction, steam is added to the hydrocarbon feedstock.

The hydrocarbon-stream mixture is heated by passing it through a tube which is suspended within a firebox. As seen in Fig. 1.7, tube units (or coils)

FIGURE 1.7 Pyrolysis tube unit being installed in steam cracker furnace.

are large. The tubes are around 100 mm diameter, with 10 mm wall thickness and about 10 m long. These tubes are expected to survive for five years or more whilst operating at wall temperatures ranging up to about 1100°C. They must therefore possess adequate resistance to creep deformation (under their own weight), to oxidation of their external surface by combustion gas and to attack by both carbon and oxygen on their inner surface.

The materials used for pyrolysis furnace tubes are centrifugally cast heat resisting steels or nickel base alloys, all austenitic alloys containing high chromium levels. Process economics are enhanced by higher operating temperatures, creating a demand for improved heat-resistant alloys. This demand has driven a shift in material selection for the centrifugally cast tubes from HK grade (25% chromium, 20% nickel) to HP grade (25% chromium, 35% nickel) steel, and more recently to alloys containing 45 or 60% nickel and around 25% chromium. These higher nickel levels are intended to achieve higher creep

strength. Consideration of the process gas composition reveals that the oxygen partial pressure is controlled by the equilibrium

$$H_2O = H_2 + \frac{1}{2}O_2 \qquad [1.9]$$

and $p_{O_2} \approx 10^{-24}$ atm at 1000°C. The carbon activity is controlled by reaction [1.8], and $a_c = 1$. Under these conditions, the main alloy constituent which is reactive is chromium, and all of the compounds Cr_2O_3, Cr_7C_3 and $Cr_{23}C_6$ are possible products. The practical findings are that an external chromium-rich oxide scale grows early in the life of the tube, but that chromium carbides precipitate within the alloy, beneath its surface, later on. The results of a laboratory simulation of the process are shown in Fig. 1.8. Questions arising from these observations on what happens to the alloy might include the following. Why do the alloy constituents other than chromium apparently not react? Why are the carbides formed as dispersed precipitates and not as scale layers? Why are carbides formed beneath the oxide and not vice versa? How does carbon penetrate the oxide layer to reach the alloy interiors? Why is there a layer of apparently unreacted alloy immediately beneath the scale? In addition, and as always, we wish to know the rates at which scale growth and internal carbide precipitation occur, and how these rates will vary with changes in temperature, alloy composition and gas conditions.

To answer these questions, it is necessary to consider first the chemical thermodynamics governing reactions between a metal and two different oxidants. Secondly, a description of the rates of mass transfer of chromium,

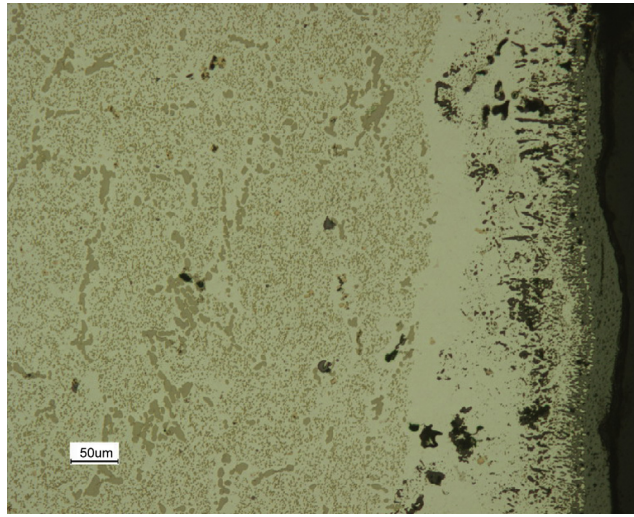

FIGURE 1.8 Cross-section of cast heat-resisting steel (HP Mod grade) after laboratory exposure to steam-hydrocarbon mixture at 1100°C for 500 cycles of one hour each.

oxygen and carbon within the solid phases is required. Finally, a knowledge of the processes whereby precipitates nucleate and grow within metals is needed, along with an ability to predict which precipitate phases can coexist with which alloy compositions.

1.5 PREDICTION AND MEASUREMENT

Emerging from a consideration of the examples above is the need to predict which reaction products result from high temperature oxidation (or carburisation, sulfidation, etc.), whether those products are formed as external scale layers or internal precipitates, how fast they form and what their mechanical stability will be, all as functions of alloy composition, temperature and gas conditions. The theoretical basis for the requisite predictive methodologies are reviewed in Chapter 2. The necessary thermodynamic, kinetic and mechanical data are not always available for complex, multicomponent systems, and further experimental investigation will be necessary. Nonetheless, theoretical prediction is still useful, as it provides qualitative indications of the expected effect of experimental variables. Even if these are no more than hypotheses, they provide a rational framework for experimental design, thereby enabling efficient planning of laboratory investigations.

At the same time, it is advisable to be aware of the possibilities afforded by modern experimental techniques. Useful theories provide predictions which can be tested, and the more thoroughly we can test a theory, the more confidence we are likely to have in it. Theoretical treatments should therefore be explored with the aim not only of achieving the desired performance predictions, but also of finding other implied outcomes which can be measured. The point here is that 'performance' in terms of component lifetime might be tens or even hundreds of thousands of hours. Other predicted results, such as compositional, microstructural or phase constitutional change in alloy or reaction product, will be evident much more rapidly. Their verification therefore provides an early indication of the probability of oxidation lifetime being achieved.

1.5.1 Oxidation Rates

The course of an oxidation reaction

$$\frac{x}{y}\mathrm{M} + \frac{1}{2}\mathrm{O_2} = \frac{1}{y}\mathrm{M}_x\mathrm{O}_y \qquad [1.10]$$

follows a kinetic rate law

$$\frac{d\xi}{dt} = f(t) \qquad [1.11]$$

where ξ is a measure of the extent of reaction at time, t. Thus

$$d\xi = dn_{M_xO_y} = -\frac{dn_M}{x} = -\frac{2dn_{O_2}}{y} \qquad [1.12]$$

where n is the number of moles. It is necessary to determine the quantitative form of the function $f(t)$.

In principle, a reaction can be followed by measuring consumption of metal or oxygen or by observing oxide accumulation, as a function of time. If the oxide is a gas, then metal consumption can be followed continuously by attaching the metal sample to a balance of appropriate sensitivity, heating it in the reaction gas and measuring the weight loss. An apparatus suitable for this experiment is shown in Fig. 1.9. In the more common case, the oxide is solid, and metal consumption cannot be directly observed in this way. Instead, a metal sample could be reacted for a time, and the amount of metal remaining after subsequent removal of the oxide measured. A series of samples reacted for different times would then yield a kinetic plot. Difficulties in removing all of the scale without damaging the underlying metal render weight change measurements of this sort inaccurate. An alternative technique is to measure the difference in metal section thickness before and after reaction. Given that the differences will be small, perhaps of order 10 μm, compared to the usual specimen thickness of some millimetres, measurement errors can be large. However, this technique has been successfully applied to the oxidation of thin foils [8].

The consumption of oxidant dn_{O_2} can be followed by observing Δp_{O_2} at constant volume, or the volume change required to maintain p_{O_2} constant. Given the vastly different densities of solids and gases, it is clear that this technique is restricted to cases of small $d\xi$, unless the oxidant can be replenished. Similar reservations apply to the use of this technique when the reaction gas is a mixture: as $d\xi$ increases, the gas changes composition.

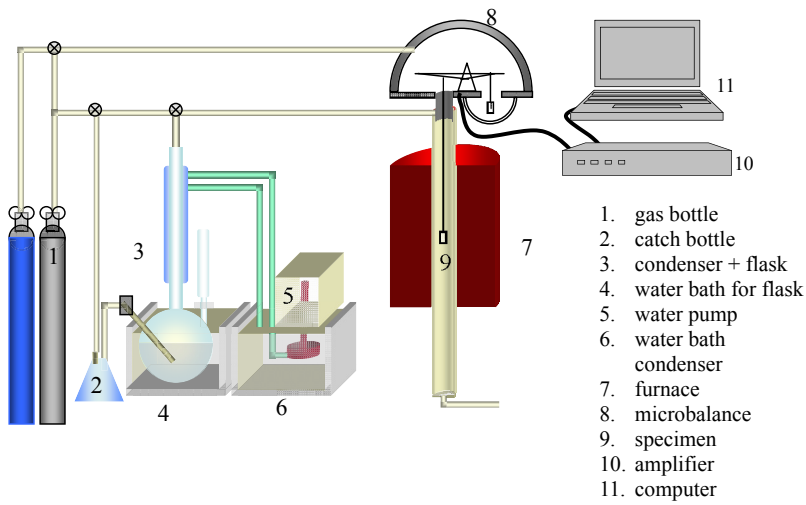

FIGURE 1.9 Schematic view of thermogravimetric apparatus for measuring weight uptake during high temperature reaction in a controlled gas atmosphere.

By far the most common method of measuring oxidation rates is the observation of oxide accumulation with time. Gravimetric measurements can be performed continuously with a microbalance or discontinuously by weighing a series of samples subjected to different reaction times. Continuous measurements yield a more accurate definition of Eq. [1.11], but the time lapse exposure approach can be used to simultaneously react a large number of different alloys. Moreover the multiple samples obtained for each alloy can be useful in characterising the reaction products. When $d\xi/dt$ is very small, the measurement precision provided by a high quality microbalance is desirable, although it can be difficult to achieve.

Microbalances are expensive. They must be protected against corrosion by the reaction gas by passing a counterflow of unreactive gas through the balance chamber, as shown in Fig. 1.9. In the case of particularly corrosive species such as SO_2 or H_2S, it is advisable to use a cheap spring balance such as that shown in Fig. 1.10. The elongation of a helical spring is observed as a sample

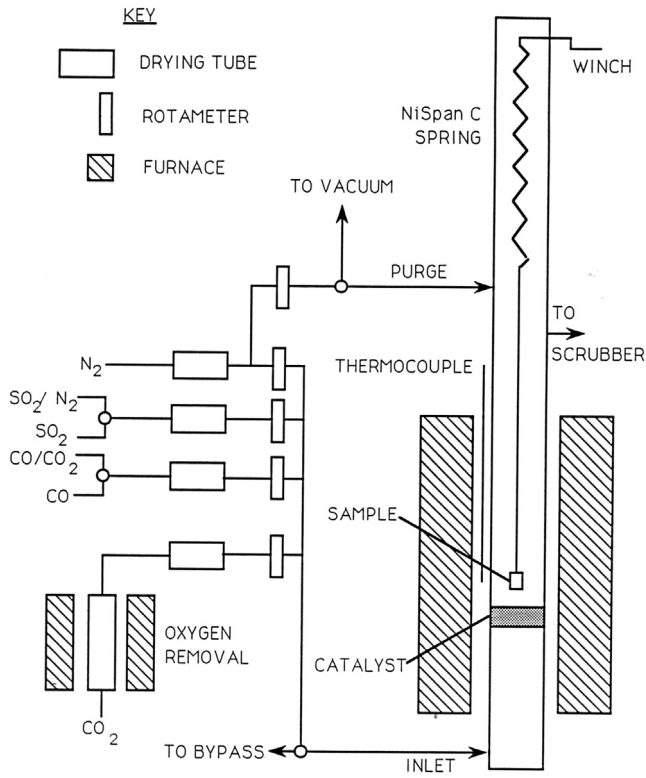

FIGURE 1.10 Schematic view of spring balance assembly for observing high temperature oxidation kinetics.

suspended from it reacts and becomes heavier. The spring is usually made from silica fibre or Ni Span C wire, the latter being an alloy with an elastic modulus insensitive to temperature.

The observed weight change, ΔW, varies with specimen surface area, A, and the measured quantity is reported as $\Delta W/A$. If no metal volatilisation occurs, the weight change corresponds to oxidant uptake, and it follows from Eq. [1.12] that

$$\frac{-2dn_{O_2}}{A} = \frac{1}{16}\frac{\Delta W}{A} = \frac{ydn_{M_xO_y}}{A} = \frac{-ydn_M}{xA} \qquad [1.13]$$

The loss of metal can then be expressed in terms of weight per unit surface area, $\Delta W_M/A$, using the atomic weight, AW_M,

$$\frac{\Delta W_M}{A} = AW_M\frac{dn_M}{A} \qquad [1.14]$$

This loss is equivalent to a decrease in volume given by

$$\frac{\Delta V_M}{A} = \frac{1}{\rho_M}\frac{\Delta W_M}{A} \qquad [1.15]$$

where ρ_M is the metal density. Recognising that uniform removal of metal from a flat surface results in a recession of the surface by a depth

$$X_M = \Delta V_M/A \qquad [1.16]$$

it is seen that

$$X_M = \frac{AW_M x}{16\rho_M y}\frac{\Delta W}{A} \qquad [1.17]$$

Similarly, the thickness X of a uniform, single-phase oxide scale grown on a flat surface can be calculated as

$$X = \frac{MW_{OX}}{16\rho_{OX}y}\frac{\Delta W}{A} \qquad [1.18]$$

where MW_{OX} is the molecular weight and ρ_{OX} the density of the oxide.

Oxide scale thicknesses can be measured directly, by examining microscopic images of cross-sections such as those shown in Figs. 1.3 and 1.8. This technique, which is described below, is relatively simple and economical. For this reason, and also because diffusion equations are expressed in terms of position coordinates, it is preferably to rephrase the general oxidation rate Eq. [1.11] as

$$\frac{dX}{dt} = f(t) \qquad [1.19]$$

1.6 RATE EQUATIONS

1.6.1 Linear Kinetics

The form of Eq. [1.19] reflects the reaction mechanism in effect. As seen in Fig. 1.2, the reaction steps can be classified within two groups: those occurring within the scale and those outside it. It might therefore be expected that steps in the latter group take place at rates independent of X. If they control the overall scaling rate, then

$$\frac{dX}{dt} = k_l \qquad [1.20a]$$

which integrates to yield

$$X = k_l t \qquad [1.20b]$$

where k_l is the linear rate constant. An example of such a situation is oxidation at very high temperatures in a dilute oxygen gas mixture. Under these conditions, diffusion in the oxide scale can be so fast that it does not contribute to rate control. However, transfer of oxygen from the bulk gas to the scale surface will be relatively slow, occurring at a rate controlled only by the gas properties, including p_{O_2} and temperature. As long as these are fixed, the rate of $O_2(g)$ arrival at the scale surface is constant, and Eq. [1.20] holds. Surface processes, such as molecular dissociation to produce absorbed oxygen [9]

$$CO_2(g) \rightarrow CO(g) + O(ad) \qquad [1.21]$$

would, if rate controlling, lead to Eq. [1.20]. Linear kinetics are expected whenever a planar phase boundary process controls the overall rate.

As noted in connection with Fig. 1.2, scale growth requires the transfer of metal and/or oxidant through the scale. If the scale is highly porous, gas phase mass transfer takes place within the pores. If the pores are large compared to the mean free path of gas molecules, their dimensions are unimportant to the rate of gaseous diffusion, and scale thickness has no bearing on the oxidation rate. Linear kinetics then result. It was pointed out by Pilling and Bedworth [10] that if the volume of oxide is less than the volume of metal consumed in the reaction, then it is likely that a porous oxide layer will result. This condition is often expressed in terms of the 'Pilling-Bedworth ratio', and the requirement for nonporous oxides is expressed as

$$\frac{V_{OX}}{xV_M} > 1 \qquad [1.22]$$

where V_i is the molar volume of the indicated species. However, a perusal of tabulated values [11] of this ratio reveals that only alkali and alkali earth metal oxides fail this test. By this criterion, all other metals should form compact scales. In fact, the situation is more complex, but it is nonetheless true that most metals of practical importance form more or less compact scales.

1.6.2 Diffusion Controlled Processes and Parabolic Kinetics

The growth rate of compact scales is commonly controlled by diffusion of some species through the scale itself. A simplified analysis of this situation is now carried out to show that rate control by such a process leads to parabolic kinetics:

$$\frac{dX}{dt} = \frac{k_p}{X} \quad [1.23a]$$

$$X^2 = 2k_p t \quad [1.23b]$$

where k_p is the rate constant.

The rate of diffusion in one dimension is described by Fick's first law [12]

$$J = -D\frac{\partial C}{\partial x} \quad [1.24]$$

Here J is the flux, which is the net rate at which the moving component passes through unit area of a plane oriented at right angles to the diffusion direction, D is the diffusion coefficient and C the concentration of a component. This equation, the physical origins of which will be examined in the next chapter, expresses the empirical fact that, other things being equal, any mobile species will flow from a region of high concentration to one where the concentration is lower, until homogenisation is achieved. The partial derivative in Eq. [1.24] is now approximated by the difference in boundary values

$$J = -D\frac{\Delta C}{\Delta x} = \frac{-D(C_2 - C_1)}{X} \quad [1.25]$$

where, as illustrated in Fig. 1.11, C_2 and C_1 are the diffusing component concentrations at the scale interfaces.

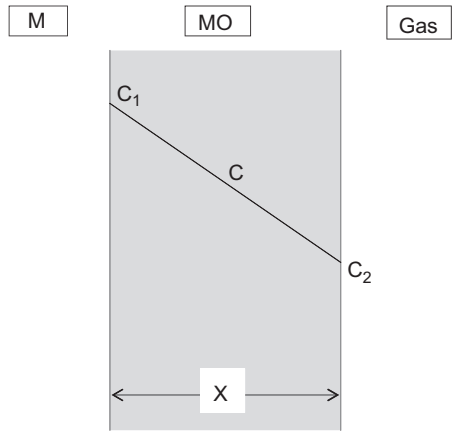

FIGURE 1.11 Simplified diffusion model for mass transport though growing scale. C represents concentration of diffusing species, and C_1, C_2 its boundary values.

If diffusion is rate-controlling, then the interfacial processes must be rapid and may be assumed to be locally at equilibrium. That is to say C_1, C_2 are time invariant. It is seen that Eq. [1.25] is equivalent in form to Eq. [1.23a], and we may write

$$k_p = \Omega D(C_1 - C_2) \qquad [1.26]$$

where Ω is the volume of oxide formed per unit quantity of diffusing species. This important result was first derived by Wagner [13], who thus showed that the scaling rate was determined by oxide properties: its diffusion coefficient and its composition when at equilibrium with metal and with oxidant. Wagner's more rigorous treatment is described in Chapter 3. Parabolic oxidation kinetics were first demonstrated experimentally by Tamman [14] and, independently, by Pilling and Bedworth [10].

Metal recession is related to oxide scale thickness through Eqs [1.17] and [1.18]

$$X_M = x\frac{V_M}{V_{OX}}X \qquad [1.27]$$

where the molar volume, V_i, of each indicated substance is equal to MW/ρ. Thus the rate equation for metal recession is

$$X_M^2 = 2k_c t \qquad [1.28]$$

with

$$k_c = (xV_M/V_{OX})^2 k_p \qquad [1.29]$$

the so-called 'corrosion rate constant'.

The rate constant measured by thermogravimetric analysis is given by

$$\left(\frac{\Delta W}{A}\right)^2 = 2k_w t \qquad [1.30]$$

For an oxide of stoichiometry M_xO_y, Eq. [1.18] can be rewritten as

$$X = \frac{V_{OX}}{16y}\frac{\Delta W}{A} \qquad [1.31]$$

Substitution in Eq. [1.30] and comparison with Eq. [1.23b] then yields

$$k_p = \left(\frac{V_{OX}}{16y}\right)^2 k_w \qquad [1.32]$$

In this book we will be concerned mainly with scale thickness and metal consumption as measures of oxidation, and will usually employ k_p and k_c.

1.6.3 Diffusion and Phase Boundary Processes Combined

Because diffusion is initially rapid, but slows with increasing scale thickness, it is possible for scale growth to be controlled in the early stages by a phase boundary reaction and later by diffusion. When the scale is thin, the scaling rate predicted from Eq. [1.23] is faster than the other processes can sustain, and the rate is instead controlled by one of them, often a phase boundary reaction. As the scale thickens, the diffusion rate eventually decreases until it becomes slower than the constant phase boundary reaction rate and then controls the overall reaction. The phase boundary process then approaches local equilibrium. The observed kinetics will be initially linear and subsequently parabolic. This behaviour has been described [15] by the rate equation

$$X_2 + LX = kt + C \qquad [1.33]$$

where L, C are constants. It is worth noting that during the initial stage, mass transfer within the scale is nonetheless occurring via diffusion, implying that the boundary values C_1 or C_2 in Eq. [1.25] change with time.

1.6.4 Volatilisation

Some metals form volatile oxides. At temperatures above about 1300°C, tungsten reacts with low pressure oxygen to form gaseous WO_3 and WO_2 species, with no solid oxide formed on the surface. If the gas composition is unchanged, metal is consumed at a constant rate. This is why incandescent light filaments, which are made of tungsten, are protected by enclosure in inert gas filled light bulbs.

A less severe situation arises with chromium, which undergoes two oxidation reactions in dry oxygen

$$2\mathrm{Cr(s)} + \frac{3}{2}\mathrm{O_2(g)} = \mathrm{Cr_2O_3(s)} \qquad [1.34]$$

$$\mathrm{Cr_2O_3(s)} + \frac{3}{2}\mathrm{O_2(g)} = 2\mathrm{CrO_3(g)} \qquad [1.35]$$

the latter reaction becoming important at temperatures above about 1000°C at $p_{O_2} = 1$ atm. The scaling rate law is then made up of two terms: diffusion controlled accumulation and a constant volatilisation loss [16]

$$\frac{dX}{dt} = \frac{k_p}{X} - k_v \qquad [1.36]$$

This equation predicts that the scale thickness increases to a steady-state value, where $dX/dt = O$ and $X = k_p/k_v$. Of course, metal continues to be lost at a constant rate proportional to k_v.

1.6.5 Thin Oxide Film Growth

During the early stages of reaction, X is very small. At low temperatures, where diffusion and other processes are slow, the time period over which X is 'thin' (ie, tens of *nanometres*) can be very long. In this regime, mass transfer through the oxide film is strongly affected by electrostatic effects. These may be understood in a qualitative way from a consideration of the schematic electron energy level diagram in Fig. 1.12. In the case of a very thin oxide film, electrons can be transferred from the underlying metal to surface levels at the oxide-gas interface by quantum mechanical tunneling through the barrier represented by the film [19]. As the film thickens, this mode of electron transport is rapidly attenuated and thermionic emission becomes the most feasible mechanism. The processes of conduction and diffusion within the film itself finally control electron transport, when scattering prevents thermionically emitted elections from crossing the film in a single step.

The electron transfer processes can be the oxide growth rate limiting processes, or they can be rapid, achieving a pseudo-equilibrium state with oxygen anions on the film surface. In the latter case, movement of charged ions (M^{n+} or O^{2-}) through the oxide film is likely to be rate controlling. The mobile ions migrate through the oxide under the influence of an electric field, E, the magnitude of which at the surface is given by Poisson's equation

$$E = 4\pi q\sigma/\varepsilon \qquad [1.37]$$

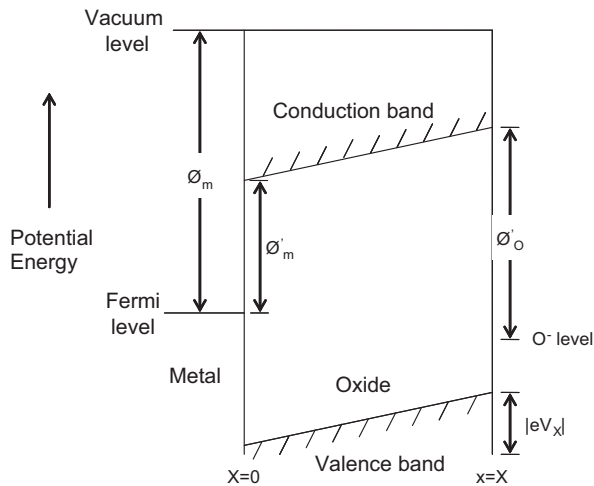

FIGURE 1.12 Approximate energy level diagram for electrons in the metal-oxide-adsorbed gas system.

where σ is the surface concentration of species with charge q, and ε is the dielectric constant of the oxide. Within the oxide the field is modified by any locally uncompensated (space) charge:

$$\frac{dE}{dx} = \frac{4\pi\rho}{x} \qquad [1.38]$$

where ρ is the space charge density. The boundary conditions for this equation are supplied by the condition of overall charge neutrality

$$E_x = \frac{4\pi q_X \sigma_X}{\varepsilon} = \frac{4\pi q_0 \sigma_0}{\varepsilon} + \int_0^X \frac{4\pi\rho}{\varepsilon} dx \qquad [1.39]$$

where the subscripts 0 and X correspond to the two film interfaces. The development of an electrostatic field during oxidation has been confirmed by surface potential measurements [17]. That the oxidation rate is affected by the magnitude of the field is confirmed by experiments [18] in which an electrostatic potential difference impressed across a growing film was shown to modify the growth rate.

At relatively low temperatures and high oxidant pressures, surface and gas phase processes are seldom rate controlling, and film thickening rates will be governed by the rate of electronic or ionic transport. The transport of all charged species depends on the electric field strength, which in turn is a function of film thickness. Evaluation of the field is achieved by integrating Poisson's Eq. [1.38], for which purpose the space charge distribution must be known. This in turn can be found from a consideration of the transport equations. At the very high field strengths prevailing in thin films, of order 10^6 V cm^{-1}, the transport equations are nonlinear, and the calculations are complex. Because this regime of behaviour is not considered in any detail in this book, the reader is referred to the comprehensive treatment provided by Fromhold [19]. A more succinct account, together with a brief review of its applicability to a selection of experimental data, is also available [20].

The first equation used to describe thin film growth kinetics was suggested by Tamman [14] as

$$X = k_1 \ln(1 + At) \qquad [1.40]$$

where k_1 and A are constants. The various theoretical treatments reviewed in Refs [19] and [20] do not lead to this expression (which was purely empirical) but instead yield for the case of rate control by ion transport equations of the form

$$dX/dt = A_1 \sinh(B_1/X) \qquad [1.41]$$

or

$$dX/dt = (A_2/X)\sinh(B_2/X) \qquad [1.42]$$

with A_i, B_i constants.

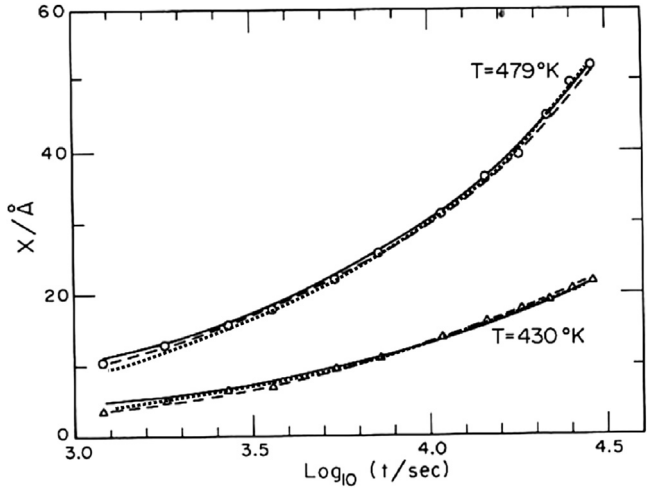

FIGURE 1.13 Zinc oxidation data and regression lines found for the sinh rate Eq. [1.41], the two-stage logarithmic Eq. [1.43] and the parabolic rate equation. *Reprinted with permission from W.W. Smeltzer, D.J. Young, Prog. Solid State Chem. 10 (1975) 17, Elsevier.*

The difficulty of distinguishing between the various models on the basis of kinetic data is illustrated in Fig. 1.13, where it is seen that when the thickness of oxide formed on zinc [21] is plotted against log (time), concave upwards curves result. This is a fairly common observation and has led to the proposal of a two-stage logarithmic rate law [22]

$$X = k_1 \ln(1 + A_1 t) + k_2 \ln(1 + A_2 t) + X_0 \qquad [1.43]$$

on the supposition that two reaction paths operate in parallel. The data in Fig. 1.13 have been curve fitted to three separate rate equations, and it is seen that their merits cannot be distinguished on this basis. It is better to test the applicability of kinetic models by seeing if the constants emerging from the fitting procedure are physically reasonable, and by verifying that the model predicts correctly the effects on reaction rate of perturbations to the system such as changes in T, p_{O_2} and E_x.

Other empirical rate laws suggested for thin film oxidation include the 'inverse log law'

$$\frac{1}{X} = \frac{1}{X_0} - k_3 \log(1 + t) \qquad [1.44]$$

and the cubic rate law

$$X^3 = k_4 t \qquad [1.45]$$

No physical basis exists for Eq. [1.44] and only under very restricted circumstances can Eq. [1.45] be justified for thin film growth [23]. However,

the cubic rate equation is found to apply to alumina scale growth (Section 5.9 of Chapter 5) when oxide grain boundaries provide the means of solid-state diffusion (Section 3.9 of Chapter 3).

1.7 REACTION MORPHOLOGY: SPECIMEN EXAMINATION

As already noted, compositional, microstructural and phase constitution information are required for both the reaction product and the nearby alloy. As seen in Fig. 1.8, these quantities can vary considerably with position in the reaction zone, and analytical methods which yield average results are inappropriate.

Many features of the reaction morphology are revealed in metallographic cross-sections, such as those made use of in this chapter. Reacted samples are embedded in cold setting epoxy resin by vacuum impregnation. After the resin cures, the section is ground and polished, usually to a 1/4 μm finish. Because the corrosion products are much more brittle than metals, additional effort is required at each stage of grinding and polishing to remove the damage remaining from the preceding step. For the same reason, it can be advantageous to protect the scale outer edge by depositing a layer of nickel or copper on it prior to sectioning. The procedure is to first vacuum evaporate or plasma coat a thin metal deposit onto the reacted sample surface, making it electrically conductive. The sample can then be electroplated with the desired thickness of metal.

The polished cross-section should first be examined by optical microscopy, using low and high magnifications, with a maximum resolution of about 1 μm. Digital images are then analysed, using image analysis computer software, to obtain data such as scale layer thickness, precipitate sizes and volume fraction, etc. The speed of this process permits extensive sampling and the accumulation of statistically reliable data. Higher magnification images can be acquired using scanning electron microscopy (SEM) or, for very high magnifications, transmission electron microscopy (TEM). Examples of the three image types are shown in Fig. 1.14.

Electron microscopy provides the opportunity to acquire compositional and crystallographic information at precisely defined locations within the reaction zone. The electron beam interacts with atoms within the sample, exciting the emission of X-rays with energies characteristic of the atomic number of the atoms involved. These X-rays are collected, analysed according to energy and counted using the technique of Energy Dispersive Analysis of X-rays (EDAX). The spatial resolution is limited by electron scattering within the solid. Depending on electron energy and their absorption by the solid, the spatial resolution is around 1−2 μm. When appropriate standards and correction procedures are used, the technique is quantitative, yielding reliable compositional analyses for metals, but only semiquantitative results for oxygen and, at best, qualitative results for carbon. The spatial resolution of EDAX is much better in

a TEM, 1−10 nm, simply because the electrons are scattered less widely during their transit of the very thin sample. The effect is illustrated in Fig. 1.15.

Superior analytical precision and the capability of analysis for light elements are provided by the alternative technique of electron probe microanalysis (EPMA). In this instrument, X-rays excited by an electron beam are analysed by

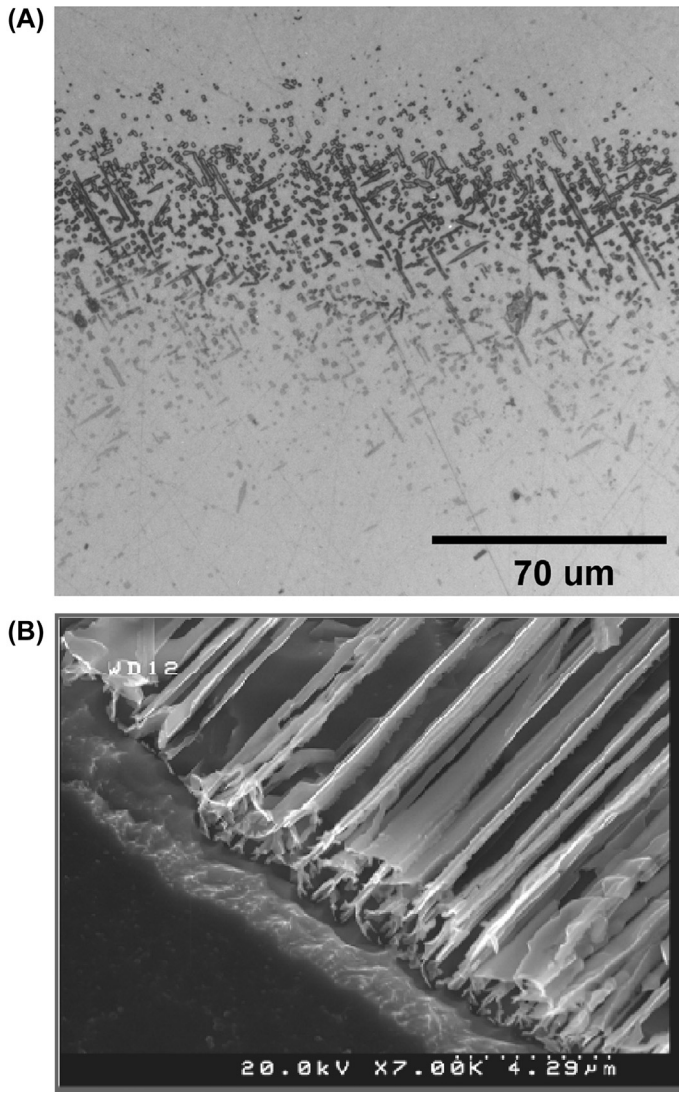

FIGURE 1.14 Section of internally carburised Fe-Ni-C alloy: (A) optical metallograph, (B) SEM view of deep-etched section, (C) TEM bright field view and (D) selected area diffraction pattern from (C).

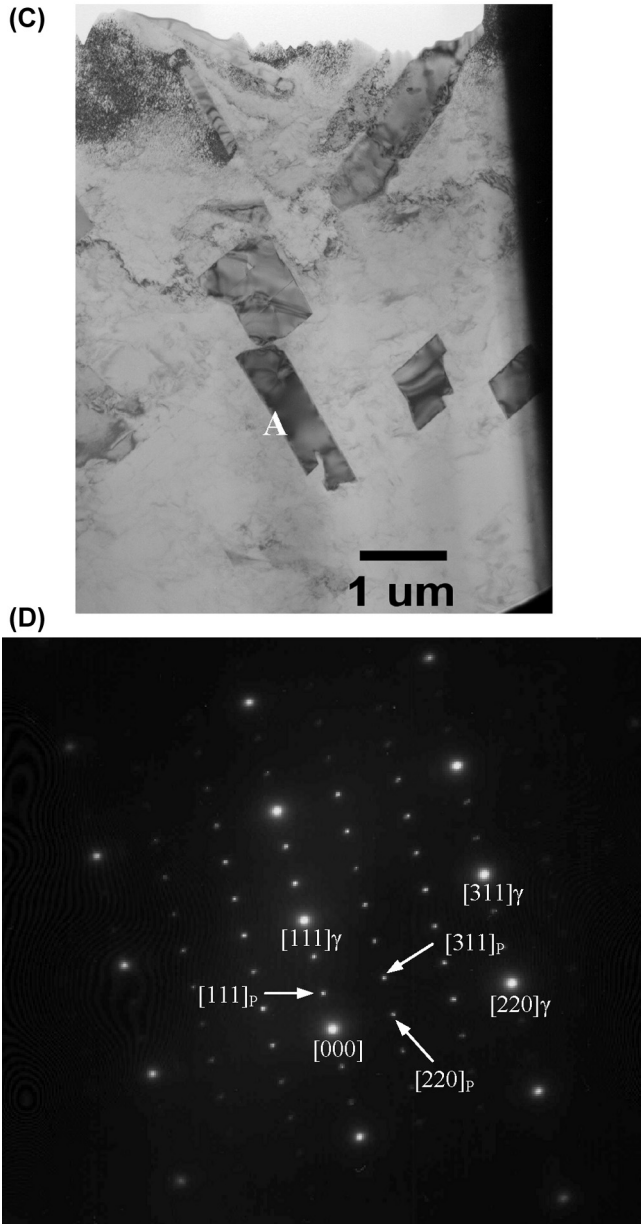

FIGURE 1.14 Cont'd.

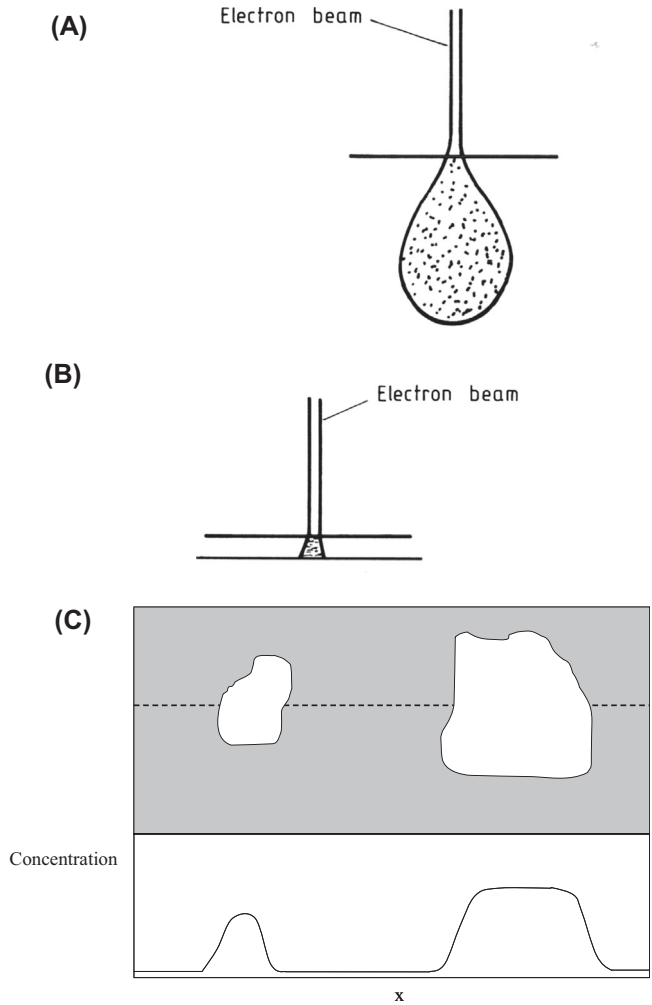

FIGURE 1.15 Spatial resolution of EDAX and EPMA limited by Compton scattering of electrons: (A) bulk sample and (B) thin foil in TEM and (C) two-phase region with corresponding analysis.

wavelength, using single crystals as diffraction gratings. This technique provides better analytical discrimination (eg, between molybdenum and sulfur) and much higher count rates.

Both EDAX and EPMA are used to identify reaction product and alloy compositions as a function of position. Care is necessary when analysing multiphase regions, such as scale−alloy interfaces or precipitate−matrix assemblages, because the electron beam can be sampling two phases at the same time. The difficulty is illustrated in Fig. 1.15, along with the remedy: 'point counting'. The beam, or preferably the sample, is stepped at small

intervals along a line intersecting the phase boundaries and X-rays counted at each point. Only when a constant composition is measured at several successive points, and when that composition is reproduced in several sample regions, can the analysis be accepted. The point-counting technique is also valuable for measuring composition profiles in scales and in underlying alloy regions.

The electron beam is diffracted by crystalline solids, and analysis of the resulting patterns provides information on the crystal structure and orientation of the diffraction region. The TEM is commonly used for this purpose, and an example is shown in Fig. 1.14. This valuable technique is now being applied more frequently to oxidised specimens, since the introduction of the focused ion beam (FIB) milling technique for producing thin foil samples for the TEM. The FIB provides thin foils in precisely determined locations and is thus able to capture interfaces, grain boundaries, etc. The SEM can also be used to generate crystallographic information via the electron back scattered diffraction (EBSD) technique. This is particularly useful for identifying alloy and oxide grain orientations, to be correlated with other reaction morphological and kinetic features.

Because SEM images can provide a large depth of field, the technique is suitable for examining rough surfaces such as the scale outer surface or the alloy surface after scale removal.

The use of electron microscopy to identify reaction product phases by diffraction can be costly and time-consuming. An alternative is provided by X-ray diffraction (XRD). The reacted sample is simply placed in the specimen holder of a diffractometer, so that the X-ray beam falls on the flat scale surface, and the intensity of diffracted beams is measured. Matching the resulting diffraction pattern with tabulated standards then leads to phase identification.

At the wavelengths and intensities normally used, X-rays penetrate only a short depth (1−3 μm) into the sample, so the technique provides information on only the near surface region. If a thin scale is being analysed, glancing angle XRD can be used to sample an extremely thin surface region. Because alloy oxidation frequently produces multiple reaction products disposed over a thick reaction zone (eg, Fig. 1.8), it is necessary to obtain diffraction data at a number of different depths. This is done by grinding away a thin surface region, obtaining an XRD pattern and repeating this process until the entire reaction zone has been traversed. This technique was used to identify the reaction products shown in Fig. 1.8: an outer scale layer of $MnCr_2O_4$ with a thicker layer of Cr_2O_3 beneath it; internal Al_2O_3 precipitates (plus some SiO_2); a single-phase austenite zone; and finally an internal carburisation zone of chromium carbide plus austenite.

The XRD technique yields measurements of crystal lattice plane spacing. Comparison of these data with those of standards reveals any distortions in the lattice, corresponding to the existence of mechanical stress. Measurements can be carried out at a high temperature to estimate stress states under reaction

conditions. Because the stress can change during a reaction, it is necessary to make very rapid measurements, and this can be done using the high intensity X-rays available from a synchrotron [24,25].

The electron beam techniques described above identify the constituent elements of a solid and define their crystallographic relationships. However, they are insensitive to atomic weight and cannot distinguish isotopes. One way of investigating the contribution of oxygen diffusion to scale growth is the use of isotopically labelled oxidants. For example, a metal can be oxidised first in $^{16}O_2$ and subsequently in $^{18}O_2$, and the scale then analysed to determine the $^{16}O/O^{18}$ distribution. If they are found to be mixed, then oxygen diffusion has occurred, whereas the observation of an $M^{18}O$ layer on top of an $M^{16}O$ layer would indicate the absence of such a process.

The necessary measurements are made by secondary ion mass spectrometry (SIMS). An ion beam is used to sputter away the scale surface, and the ejected ions are analysed by mass spectrometry. Sputtering is continued, removing successively deeper regions of oxide, until the underlying metal is reached. An example of the results obtained in this way is shown in Fig. 1.16.

Another technique sensitive to atomic mass is atom probe tomography (APT). Very small needle shaped tips (radius of curvature ~10 nm) are milled from the material of interest and subjected to a strong electrostatic field. The field strength is such that, with the assistance of laser energy pulses, ions are emitted from the tip. These are identified by mass spectrometry, and their trajectories used to calculate their origin in the specimen. A three-dimensional analysis of the material with atom scale resolution results. This technique has [27,28] been applied to oxide scales, yielding remarkably detailed information.

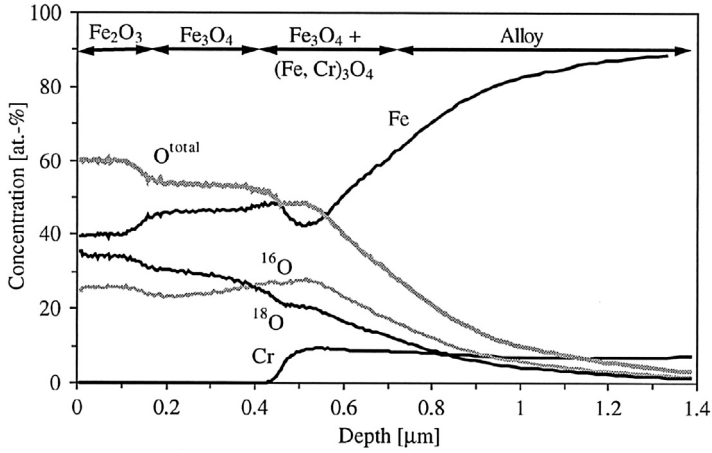

FIGURE 1.16 SIMS analysis of scale grown on an Fe-9Cr steel in $N_2-1\%^{16}O_2-2\%H_2{}^{18}O$ showing different extents of oxidation by O_2 and H_2O in different parts of the scale. *Reprinted with permission from J. Ehlers, D.J. Young, E.J. Smaardijk, A.K. Tyagi, H.J. Penkella, L. Singheiser, W.J. Quadakkers, Corros. Sci. 48 (2006) 3428, Elsevier.*

1.8 SUMMARY

As seen from the oxidation cases examined here, a diversity of oxidation reaction morphologies and rates is possible. It is important, therefore, to be able to predict under which circumstances (alloy composition and environmental state) each particular form of reaction will occur, the kinetics of the process and how the rate varies with temperature and the compositions of both alloy and gas. An understanding of these fundamental principles then permits a rational approach to materials selection (or design), and the determination of suitable operating limits for temperature, gas composition, flow rate, etc.

Two basic techniques are used to approach the problem. Chemical thermodynamics are employed to predict the reaction outcome, and an analysis of mass transfer processes provides an evaluation of reaction rate. The enabling theory underlying these techniques is summarised in Chapter 2, and examples relevant to high temperature oxidation are discussed. In addition, summary descriptions are provided for interfacial processes and the effects of mechanical stress in oxide scales.

REFERENCES

[1] J.S. Sheasby, W.E. Boggs, E.T. Turkdogan, Met. Sci. 18 (1984) 127.
[2] L. Himmel, R.F. Mehl, C.E. Birchenall, Trans. AIME 197 (1953) 822.
[3] V.H.J. Lee, B. Gleeson, D.J. Young, Oxid. Met. 63 (2005) 15.
[4] F.H. Stott, N. Hiramatsu, Mater. High Temp. 17 (2000) 93.
[5] C.T. Sims, N.S. Stoloff, W.C. Hagel (Eds.), Superalloys II, Wiley-Interscience, New York, 1987.
[6] G.W. Goward, in: R.A. Rapp (Ed.), High Temperature Corrosion, NACE, Houston, 1983, p. 553.
[7] B. Gleeson, J. Propul. Power 22 (2006) 375.
[8] B.A. Pint, J. Eng. Gas Turbines Power 128 (2006) 370.
[9] F.S. Pettit, R. Yinger, J.B. Wagner, Acta Met. 8 (1960) 617.
[10] N.B. Pilling, R.E. Bedworth, J. Inst. Met. 29 (1923) 529.
[11] O. Kubaschewski, B.E. Hopkins, Oxidation of Metals and Alloys, Butterworth, London, 1953.
[12] A.E. Fick, Pogg. Ann. 94 (1855) 59.
[13] C. Wagner, Z. Phys. Chem. 111 (1920) 78.
[14] G. Tammann, Z. Anorg. Chem. 111 (1920) 78.
[15] P. Kofstad, High Temperature Corrosion, Elsevier, London, 1988.
[16] C.S. Tedmon, J. Electrochem. Soc. 113 (1966) 766.
[17] F.P. Fehlner, N.F. Mott, Oxid. Met. 2 (1970) 59.
[18] P.J. Jorgensen, J. Electrochem. Soc. 110 (1963) 461.
[19] A.T. Fromhold, Theory of Metal Oxidation, Elsevier, New York, 1975.
[20] W.W. Smeltzer, D.J. Young, Prog. Solid State Chem. 10 (1975) 17.
[21] V.O. Nwoko, H.H. Uhlig, J. Electrochem. Soc. 112 (1965) 1181.
[22] I.M. Ritchie, Surf. Sci. 23 (1970) 443.
[23] D.J. Young, M.J. Dignam, Oxid. Met. 5 (1972) 241.

[24] P.F. Tortorelli, K.L. More, E.E. Specht, B.A. Pint, P. Zschack, Mater. High Temp. 20 (2003) 303.
[25] P.Y. Hou, A.P. Paulikas, B.W. Veal, Mater. Sci. Forum 522–523 (2006) 433.
[26] J. Ehlers, D.J. Young, E.J. Smaardijk, A.K. Tyagi, H.J. Penkella, L. Singheiser, W.J. Quadakkers, Corros. Sci. 48 (2006) 3428.
[27] D.J. Young, T.D. Nguyen, P. Felfer, J. Zhang, J.M. Cairney, Scripta Mater. 77 (2014) 29.
[28] F. Liu, M. Halvarsson, K. Hellstrom, J.-E. Svensson, L.-G. Johansson, Oxid. Met. 83 (2015) 441.